Journal of Asian Earth Sciences 132 (2016) 25–39

Contents lists available at ScienceDirect

Journal of Asian Earth Sciences

journal homepage: www.elsevier.com/locate/jseaes

Full length Article

Two crustal flowing channels and volcanic magma migration underneath the SE margin of the Tibetan Plateau as revealed by surface wave tomography

Tengfei Wu [a,c], Shuangxi Zhang [a,b,c,*], Mengkui Li [a], Weibing Qin [a], Chaoyu Zhang [a,b]

[a] Department of Geophysics, School of Geodesy and Geomatics, Wuhan University, Wuhan 430079, China
[b] Key Laboratory of Geospace Environment and Geodesy of Ministry of Education, Wuhan University, Wuhan 430079, China
[c] Collaborative Innovation Center of Geospace Information Science, Wuhan University, Wuhan 430079, China

ARTICLE INFO

Article history:
Received 5 May 2016
Received in revised form 22 September 2016
Accepted 23 September 2016
Available online 24 September 2016

Keywords:
Surface wave tomography
S-wave velocity structure
Crustal flow
Volcanic magma migration
Tengchong volcano
Tibetan Plateau

ABSTRACT

The SE margin of the Tibetan Plateau is an important area to develop a better understanding of the plateau uplift and the Indian-Eurasian continental collision dynamics. Previous studies have reported widespread low-velocity anomalies beneath this region, particularly in the Tengchong volcanic field (TCVF). However, the spatial distribution and dynamic processes of these low-velocity anomalies are not well constrained. In this study, a 3-D S-wave velocity structure model of the crust and upper mantle (10–120 km) in the region is constructed by the inversion of surface wave dispersion data. A two-step inversion procedure is adopted to generate the S-wave velocity structure images. The measured phase velocities and inverted S-wave velocities jointly show a large-scale low-velocity anomaly distributed in the crust, consistent with the view that the region is the passageway of the eastward migration of Tibetan Plateau material. Two crustal flowing channels are clearly observed at depths of ~20 km and ~30 km, which connect and rotate clockwise around the Eastern Himalaya Syntaxis. Beneath the TCVF, there are two prominent low-velocity anomaly zones at depths of ~15–25 km and ~50–80 km, which indicate the existence of magma chambers. One of the crustal flowing channels is connected with the magma chamber of the TCVF, and the other has a short branch north of Kunming toward the Mile-Shizong fault at a depth of 20 km. Based on the distribution of the S-wave velocities under the TCVF, a dynamic model of the Tengchong volcano magma system is proposed to explain the migration patterns of the volcanic material.

1. Introduction

The Tibetan Plateau was formed by the continent-continental collision of the Indian and Eurasian plates during the Cenozoic era, which began ~50 Ma ago (Molnar and Tapponnier, 1975; Rowley, 1996; Yin and Harrison, 2000). The geological evolution of the Tibetan Plateau has been the focus of numerous studies (Tapponnier et al., 1982, 2001; England and Houseman, 1986; Clark and Royden, 2000; Yin and Harrison, 2000; Decelles et al., 2002; Royden et al., 2008; Huang et al., 2015; Li et al., 2016). The deformation mechanisms of the Tibetan Plateau and the geodynamic processes of the continental collision are still matters of debate (Clark and Royden, 2000; Tapponnier et al., 2001; Royden et al., 2008; Yao et al., 2010; Huang et al., 2015). In the SE margin of the Tibetan Plateau and its surrounding areas to the east, the regional deformation is the consequence of the northward subduction of the Indian plate and the eastward subduction of the Burma microplate with the resistance of the Sichuan Basin, leading to high-level seismicity and volcanic activity (Fig. 1; Ni et al., 1989; Shen et al., 2003; Qiao et al., 2004; Schoenbohm et al., 2004; Cook and Royden, 2008; Lei et al., 2009; Zhao and Liu, 2010; Zhang et al., 2016). In addition, as an important part of the SE front of the Tibetan Plateau, the region has been regarded as the pathway of Tibetan Plateau material moving southeast (Bai et al., 2010; Zhao et al., 2013; Chen et al., 2014b; Bao et al., 2015; Li et al., 2016). Therefore, this region provides an ideal place for a better understanding of the mechanism of plateau uplift and the lithospheric dynamics of the Indian-Eurasian continental collision.

Seismic tomography has been considered the most effective tool for investigating the deep structure of the Earth (Simons et al., 1999; Danesi and Morelli, 2001; He et al., 2005; Shapiro

* Corresponding author at: Department of Geophysics, School of Geodesy and Geomatics, Wuhan University, Wuhan 430079, China.
E-mail address: shxzhang@sgg.whu.edu.cn (S. Zhang).

http://dx.doi.org/10.1016/j.jseaes.2016.09.017
1367-9120/

et al., 2005; Yao et al., 2006, 2008; Zhao, 2009; Zhang and Wang, 2009; Zhao et al., 2011; Huang et al., 2013; Chen et al., 2014a). Other geophysical methods used to study the lithospheric structure, include the receiver function (Li et al., 2014b; Li et al., 2016), magnetotelluric imaging (Wei et al., 2001; Bai et al., 2010) and others. Previous studies have indicated the existence of low-velocity anomalies in the crust of the SE margin of the Tibetan Plateau (Huang et al., 2002; Li et al., 2008b; Bai et al., 2010; Yao et al., 2010; Chen et al., 2014b; Bao et al., 2015), but the geometric details of these anomalies are not clear. Li et al. (2008b) found that low-velocity anomalies exist in the middle-to-lower crust beneath the Yunnan region, SE Tibet. Bai et al. (2010) identified two crustal flowing channels with high conductivities extending from the Tibetan Plateau to the region east of it. Chen et al. (2014b) observed two disconnected low-velocity channels in the crust beneath the SE Tibetan Plateau. Li et al. (2016) found two low-velocity zones in the middle-to-lower crust of the SE Tibetan Plateau, and they are connected in southern region of the SE Tibetan Plateau. Their studies both revealed the presence of two possible crustal flowing channels in the SE Tibetan Plateau. However, the geometric features and geodynamic processes of two low-velocity channels are not clear. In addition, the Tengchong volcano is the only active volcano at the Indian-Eurasian continental collision zone (Zhou et al., 2012; Zhang et al., 2016). Seismic tomographic studies revealed a broad low-velocity anomaly distributed in the crust and upper mantle (Liu et al., 1993; Li et al., 2008a; Lei et al., 2009; Wang and Huangfu, 2004; Huang and Zhao, 2006), suggesting the presence of magma chambers beneath the Tengchong volcanic field (TCVF).

P-wave tomography is a widely used technique to map large-scale geological structures (Huang et al., 2002; Wang and Huangfu, 2004; Lei et al., 2009; Wei et al., 2012; Xu et al., 2012). In addition, surface waves have become indispensable information used for the tomographic imaging of S-wave velocity structures (He et al., 2004). In reference to the geological setting of the TCVF, some studies (e.g., Huang et al., 2002; Huang and Zhao, 2006; Wang et al., 2003; Wang and Huangfu, 2004; Lei et al., 2009) have revealed the existence of a low-velocity anomaly at the crustal and upper mantle depth. However, the spatial position and possible origin of the magma chamber is still being debated.

This study aims to investigate the 3-D S-wave velocity structure model of the crust and upper mantle (10–120 km) beneath the SE margin of the Tibetan Plateau. The high-density ray paths are extracted from 755 teleseismic events and long-term continuous

Table 1
Instrument types in the study region.

Station type	Seismometer type	Collector type	Corner frequency	Number
Yunnan Monitoring Network	BBVS60, 120	EDAS-24IP	50 Hz–60 s, 120 s	19
	KS2000	EDAS-24IP	50 Hz–60 s	16
	CTS-1	EDAS24-L6	50 Hz–60 s	8
	GL-S60	EDAS-IP	50 Hz–60 s	5
Tengchong volcano Monitoring Network	KS2000	EDAS-24P	50 Hz–60 s	8
	CTS-1	EDAS-24P	50 Hz–60 s	1

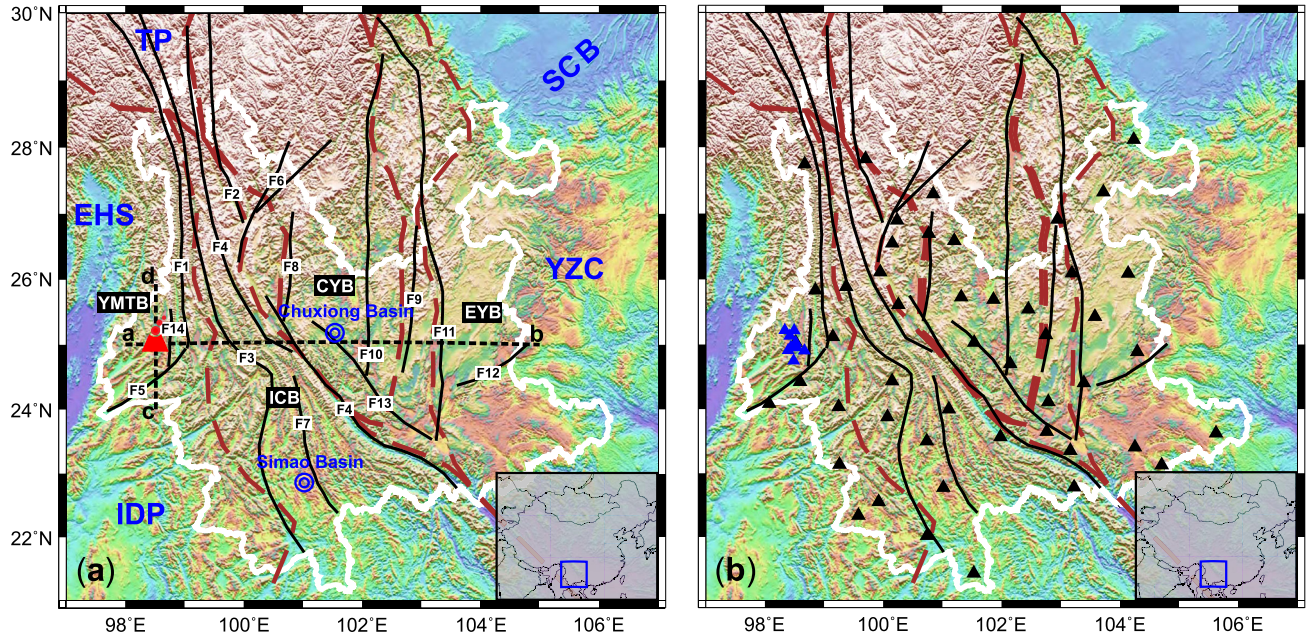

Fig. 1. (a) Geologic background. The solid white lines denote the boundaries of the Yunnan province, SE margin of the Tibetan Plateau. The red triangle and red circle denote Tengchong volcanoes. The two blue concentric circles represent the locations of the Simao basin and the Chuxiong basin. The brown dashed lines are the boundaries between the major blocks, and the black solid lines represent faults. (Total of four Blocks: YMTB, Yunnan-Myanmar-Thailand Block; ICB, Indo-China Block; CYB, Central Yunnan Block; and EYB, East Yunnan Block; and fourteen major faults: F1, Nujiang fault (NJF); F2, Zhongdian fault (ZDF); F3, Lancangjiang fault (LCJF); F4, Red River fault (RRF); F5, Longling fault (LLF); F6, Lijiang-Ninglang fault (LJNLF); F7, Wuliangshan fault (WLSF); F8, Chenghai fault (CHF); F9, Puduhe fault (PDF); F10, Yimen fault (YMF); F11, Xiaojiang fault (XJF); F12, Mile-Shizong fault (MLSZF); F13, Chuxiong-Tonghai fault (CXTHF); and F14, Tengchong fault (TCF)). TP, Tibetan Plateau; EHS, Eastern Himalaya Syntaxis; IDP, Indian Plate; SCB, Sichuan Basin; and YZC, Yangtze Craton. The black dashed lines are the two profiles that are discussed in the volcanic structure. (b) Distributions of seismic stations. Black triangles and blue triangles denote the Yunnan Monitoring Network and the Tengchong volcanic field (TCVF) Monitoring Network, respectively. The boundary data of the faults and blocks are adopted from Wang and Gao (2014). (For interpretation of the references to colour in this figure legend, the reader is referred to the web version of this article.)

observations recorded by 57 local broadband seismic stations. A two-step inversion procedure is used to invert the S-wave velocity image of the region. In the first step, the distributions of the Rayleigh wave phase velocities at different periods are determined from the corresponding dispersion data. In the second step, the 1-D S-wave velocity structures are inverted at each grid node and are subsequently interpolated to generate the 3-D S-wave velocity structure of the studied region.

2. Waveform data and methodology

2.1. Data selection

In this study, the seismic data records were collected from 57 seismic stations in the SE margin of the Tibetan Plateau, of which 48 stations are operated by the Yunnan Monitoring Network and 9 stations by the Tengchong volcano Monitoring Network. The teleseismic data include records from January 2012 to June 2015. Instrument types and stations distribution are shown in Table 1 and Fig. 1b, respectively. The dispersion curves are extracted from 755 selected teleseismic events (Fig. 2). All seismic events are selected using the following criteria: The epicenter distances are between 20° and 90°, the moment magnitude of events are 5.5–7.5 to prevent near-source effects and interference from higher modes of surface waves, and the epicenter depth is less than 100 km, which ensures the sufficient development of surface waves. To extract the high-quality dispersion curves, the waveforms are selected based on the following basic criteria: first, the selected angles α and β are less than 3° and 5° (see Fig. 12 in Yao et al., 2006), respectively. Here, α is the azimuthal difference of the earthquake to the station pairs, and β is the azimuthal difference between the earthquake to the station and the station to another station. It is noted that angles α and β should be small enough so that the station pairs and the earthquake source are approximately on the same large circle (Deschamps et al., 2008). Next, the stations are more than 100 km apart to reduce short-period measurement errors. Finally, the selected event waveforms must be of signal-to-noise ratio (SNR) higher than 5.0.

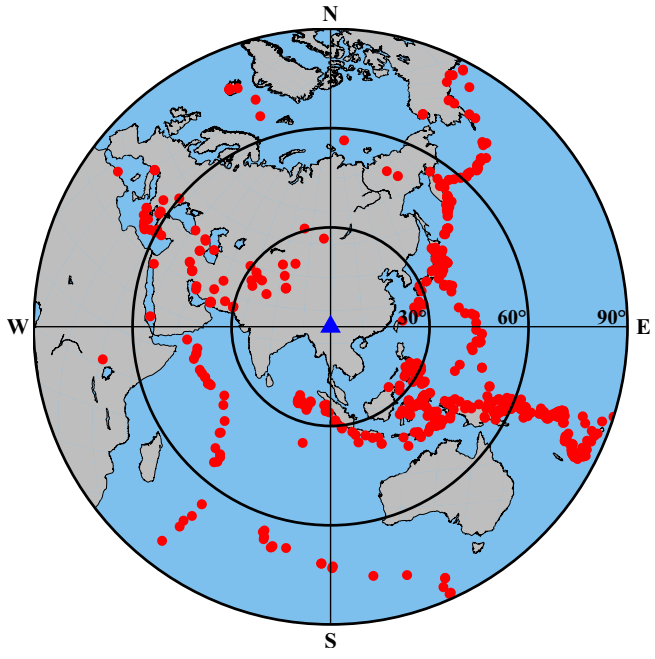

Fig. 2. Azimuthal distribution of the 755 teleseismic events used in this study. The blue triangle in the center denotes the study area. The digits indicate the distances from the center. The red dots denote the epicenter locations of the earthquakes, most of the events are from the direction of the Pacific Ocean, but they still have a good azimuthal coverage. (For interpretation of the references to colour in this figure legend, the reader is referred to the web version of this article.)

2.2. Dispersion data construction

The phase velocity dispersions are extracted using the two-station method (Yao et al., 2005). Fig. 3 shows the example of stations BAS and QIJ for the Mw 6.2 earthquake (39.85°N, 142.88°E and 23 km deep) on February 16th, 2015 that occurred in Miyako, Japan. The following processing steps are performed:

(1) Making a zero-drift correction to the interstation waveforms $s_1(t)$ and $s_2(t)$ from the two stations for the same seismic event, removing their instrument responses, and normalizing the waveforms (Fig. 3a).
(2) Using the multiple filter technique (MFT) method to determine each station's arrival times, $t_{g1}(T_c)$ and $t_{g2}(T_c)$, for the group velocity of the fundamental mode of the Rayleigh waves, where T_c is the period (Fig. 3b).
(3) Filtering the two waveforms with a narrow band-pass filter with a variable moving time-window to obtain the harmonic waves with the same frequency. The narrow band-pass filter had the following expression:

$$yi(t,T_c) = [si(t) \times w(t,T_c) * hd(t,T_c)] \quad i = 1,2,\ldots \tag{1}$$

where $yi(t,T_c)$ is the narrow band-pass filtering result of the i-th station's waveform record with a variable moving time-window. $hd(t,T_c)$ is the narrow band-pass filter of a finite impulse response with a Kaiser window and a Kaiser window parameter selection range of 5–10; the effect of the band-pass filtering appeared to be good. $w(t,T_c)$ is a time window with a cosine shoulder (Eq. (2)):

$$w(t,T_c) = \begin{cases} 1 & t_{gi}(T_c) - nT_c < t < t_{gi}(T_c) + nT_c \\ \cos\left(\pi \times \frac{|t - t_g(T_c) - nT_c|}{T_c}\right) & -T_c/2 < |t - t_{gi}(T_c)| - nT_c < T_c/2 \\ 0 & elsewhere \end{cases} \tag{2}$$

where n is a window constant with typical value of 2–4. First, we apply this taper window $w(t,T_c)$ to the waveform to separate the fundamental-mode surface wave and eliminate the influence of higher-order mode surface waves to improve the accuracy of the extracted phase velocities. Next, the cross-correlation amplitude image is obtained for each interstation pair after cross-correlating the two filtered seismograms. Finally, the dispersion curve is chosen using the quick tracing method, and a three-spline interpolation is performed to transform the cross-correlation amplitude image into a phase velocity image (Fig. 3c).

We obtained more than 1400 high-quality phase velocity dispersion curves successfully with this strategy. Fig. 4 shows the number of paths for different periods. For most periods, there are more than 1000 ray paths. Compared to previous studies (i.e., He et al., 2005), the path density has improved significantly. Fig. 5 shows the average phase velocity dispersion curves for Rayleigh waves in the study area. Comparing these curves with the global dispersion curve model, the observed average phase velocity of the study region is much slower than the 1-D average model AK135. This may be due to the crust being thicker than the average global crust (Fan et al., 2015). Another possibility is that the region crustal rock is widely weakened and fractured. Fig. 6 shows the path coverage maps at 10, 15, 30 and 60 s, and most study areas have good path coverage.

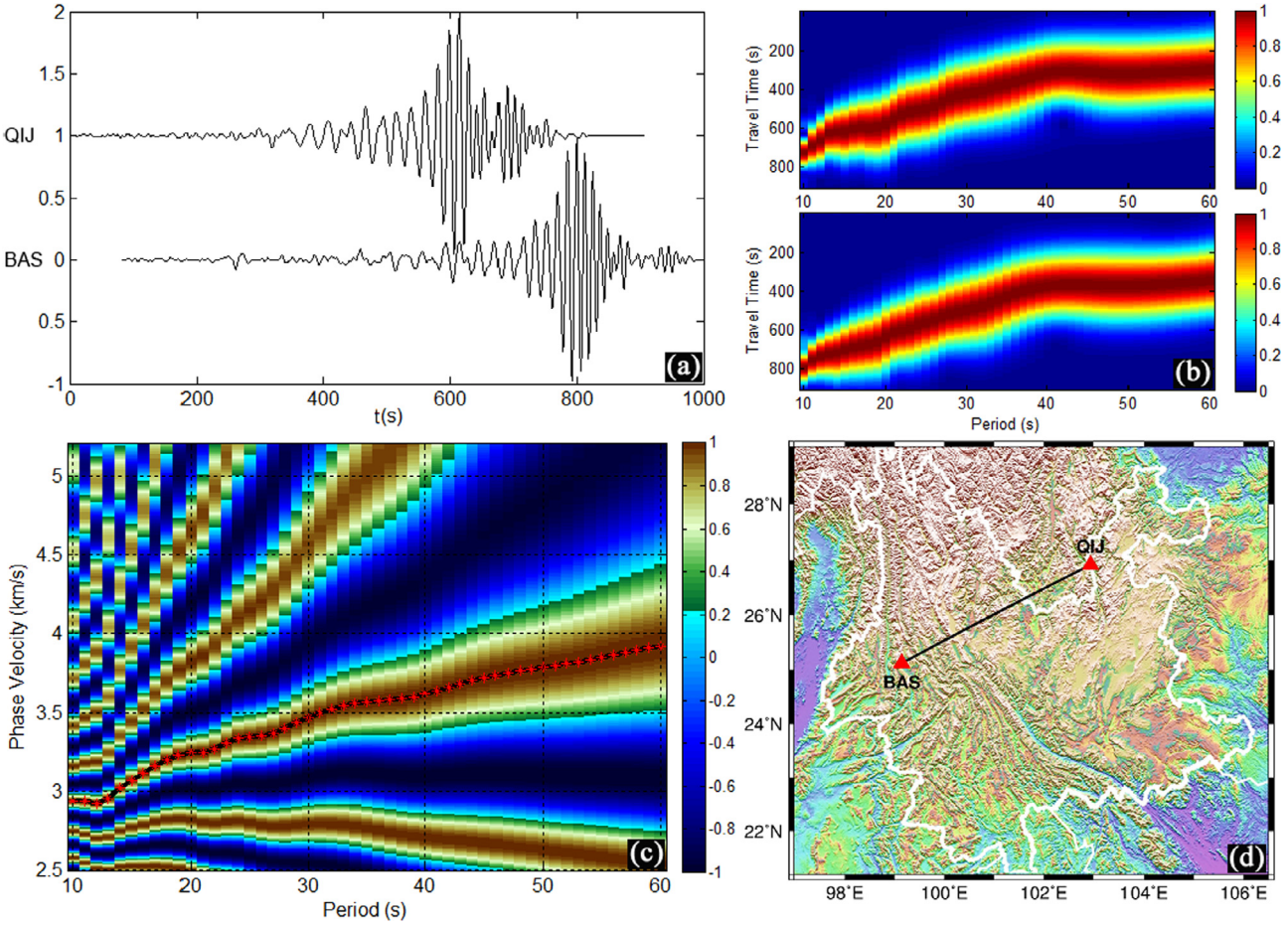

Fig. 3. The phase velocity dispersion curve extracted from the interstation records of BAS and QIJ. (a) Two station cross-correlation waveform records; (b) Group wave travel times from the MFT; (c) Dispersion curve picking; and (d) Locations of stations BAS and QIJ.

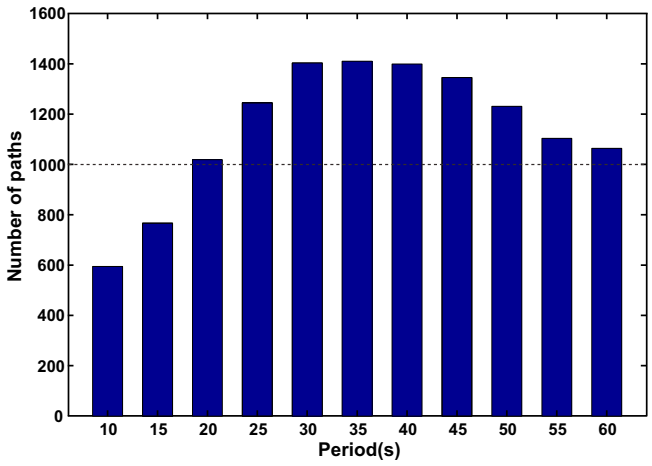

Fig. 4. Numbers of interstation phase velocities at different periods used for tomographic inversion. The abscissa represent periods and the ordinate denote the numbers of ray paths. At 20–60 s, the number of paths is more than 1000.

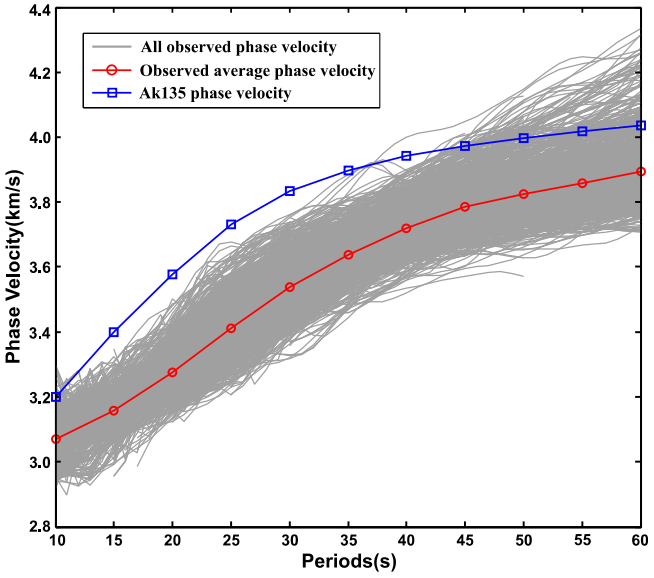

Fig. 5. The average phase velocity dispersion curves of the Rayleigh wave. The grey solid lines are the dispersion curves selected for the inversion of the Rayleigh-wave phase velocity of the study region. The red solid line represents their average. The blue line is the predicted phase velocity calculated from a 1-D reference Earth model AK135 (Kennett et al., 1995). (For interpretation of the references to colour in this figure legend, the reader is referred to the web version of this article.)

2.3. Tomographic inversion of the rayleigh wave phase velocities

For each pair of stations, we may extract the interstation dispersion curve for each seismic event. A generalized 2-D linear inversion method (Ditmar and Yanovskaya, 1987; Yanovskaya and Ditmar, 1990) is adopted to construct the phase velocity images for different periods (Ritzwoller and Levshin, 1998; Fang et al., 2010; Li et al., 2010, 2013; Yu et al., 2016). This inversion method

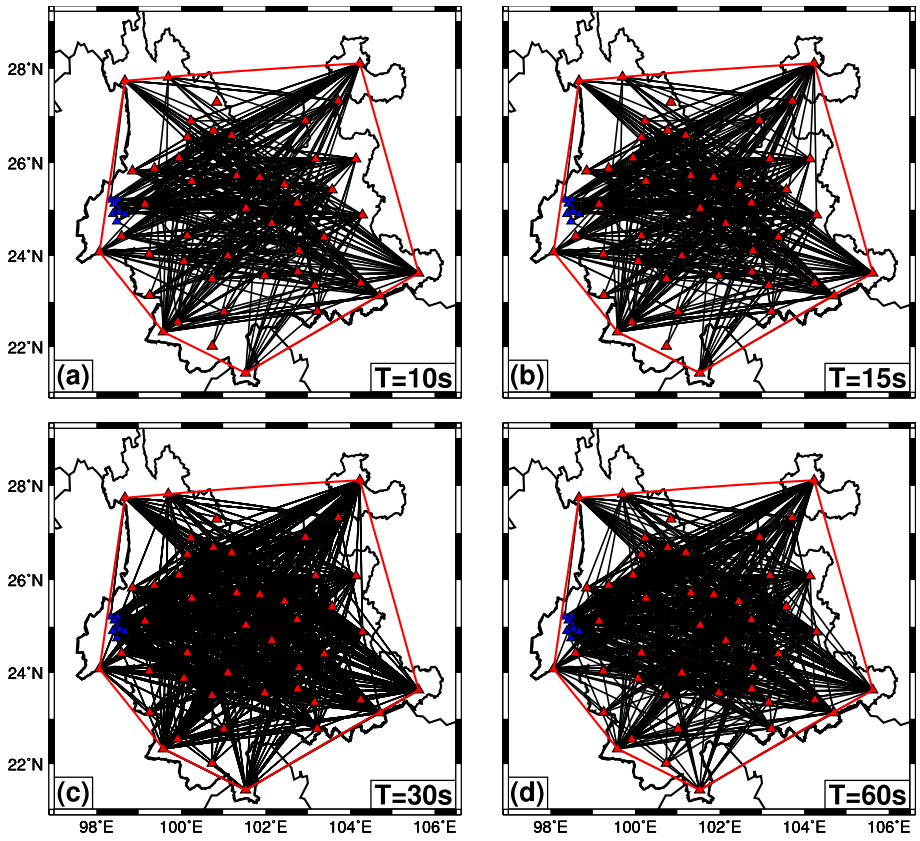

Fig. 6. Accepted interstation path coverage of the Rayleigh wave phase velocity at 10, 15, 30 and 60 s. The location map of the region shows seismic array station locations and accepted interstation paths after SNR examination. The red solid polygon shows that the area has good ray coverage. (For interpretation of the references to colour in this figure legend, the reader is referred to the web version of this article.)

is based on the assumption of the smoothness of the velocity $C(x)$ according to the following misfit function:

$$(d - Gm)^T (d - Gm) + \alpha \iint |\nabla m(x)|^2 dx = \min \tag{3}$$

where

$$m(x) = \left[C^{-1}(x) - C_0^{-1}\right] \tag{4}$$

$$d_i = T_i - T_{i0} \tag{5}$$

$$(Gm)_i = \iint G_i(x) m(x) dx = \int_{L_{0i}} m(x) \frac{ds}{C_0} \tag{6}$$

and

$$\iint G_i(x) dx = \int_{L_{0i}} \frac{ds}{C_0} = t_{i0} \tag{7}$$

In Eqs. (3)–(7), $x = x(\theta, \varphi)$ is the position vector, C_0 is the initial velocity corresponding to the starting model, T_i is the observed travel time along the i-th path, T_{i0} is the travel time calculated from the staring model, L_{i0} is the length of the i-th path, S is the path of performed inversion, and α is a regularization parameter, controlling the trade-off between the best fitting and the smoothness of the resulting phase velocity images. Traditionally, the calculation of the regularization parameter is based on the L-curve method (Hansen, 1998), which is quasi-optimal corresponding to the corner in L-curve. Here, the phase velocities are tested by several regularization parameters, such as $\alpha = 0.1, 0.15, 0.2, 0.25$ and 0.3, which are derived from the recommended values (~0.1–0.3) of the inversion software developer, among which $\alpha = 0.2$ produced relatively smoother maps with smaller solution errors than the others. This value is also referred to in other trials (Fang et al., 2010; Wang et al., 2012, 2014; Pan et al., 2015). The following tomographic calculations are thus conducted using $\alpha = 0.2$ to ensure phase velocity results with good smoothness.

Following the strategy of Yanovskaya (1997) and Yanovskaya et al. (1998), who used the mean size of the averaging area to estimate the resolution of the data, we estimate the anomaly area. The details may refer to certain studies (e.g., Yanovskaya, 1997; Yanovskaya et al., 1998; Fang et al., 2010; Wang et al., 2012). Utilizing this method, we obtained the resolution maps at periods of 10, 15, 30 and 60 s (Fig. 7). The results show that the central part of the study area has a resolution of approximately 40–50 km, and the border area has a resolution of approximately 70–100 km.

To further verify the validity of our tomographic results, we perform checkerboard resolution tests (Fig. 8). First, we create $1° \times 1°$ grids in the synthetic phase velocity model in the study region with ±6% velocity disturbances of the average phase velocity for each period. Next, the synthetic travel times along the interstation paths are calculated with an additional 1.5% of random noise. Ultimately, we invert the synthetic velocity model by using the same inversion parameters as with the real data to obtain the retrieve model. Fig. 8 shows the checkerboard test results at 10, 30 and 60 s. The checkerboard resolution tests indicate that the input anomalies can be retrieved reasonably in most part of the study region. In particular, the lateral resolution in the center is able to reach ~0.5°, namely, half of the width of the checkerboard (Lebedev and Nolet, 2003; Li et al., 2014a). However, the surrounding area is not well resolved due to relatively poor path coverage, especially in the short periods (e.g., T = 10 s). Our resolution test results obtained from the mean size of the averaging area and

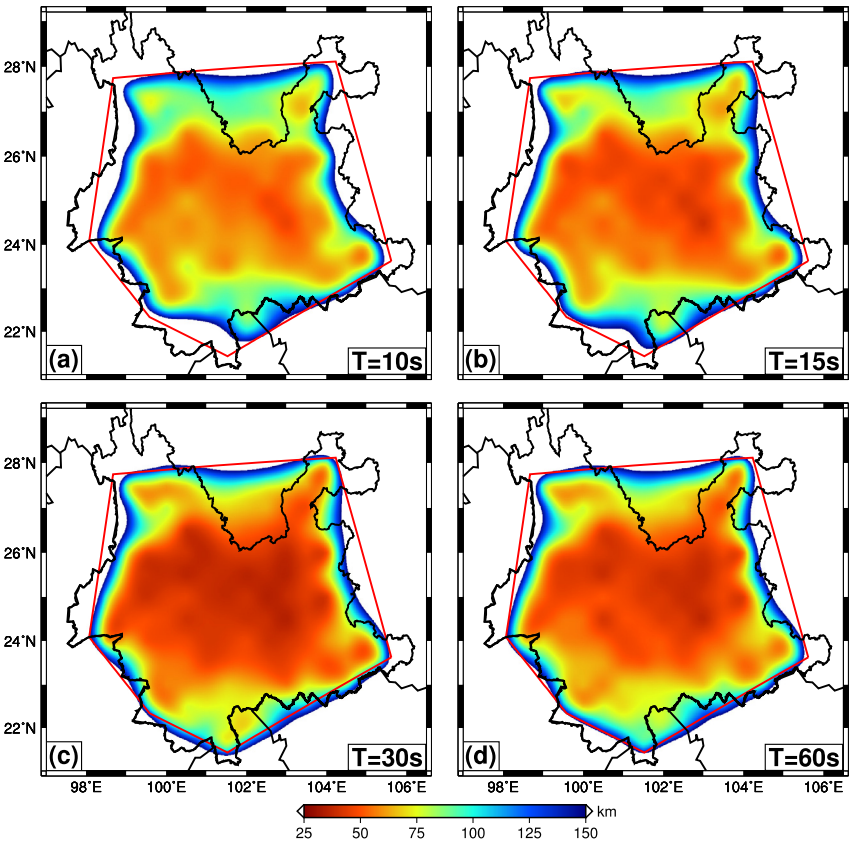

Fig. 7. Resolution maps are obtained from the mean size of the averaging area at 10, 15, 30 and 60 s. Resolution is defined as twice the standard deviation of a 2-D Gaussian function that is fit to the resolution matrix at each point (Levshin et al., 2005). Most of the region can reach a resolution of ~40–50 km.

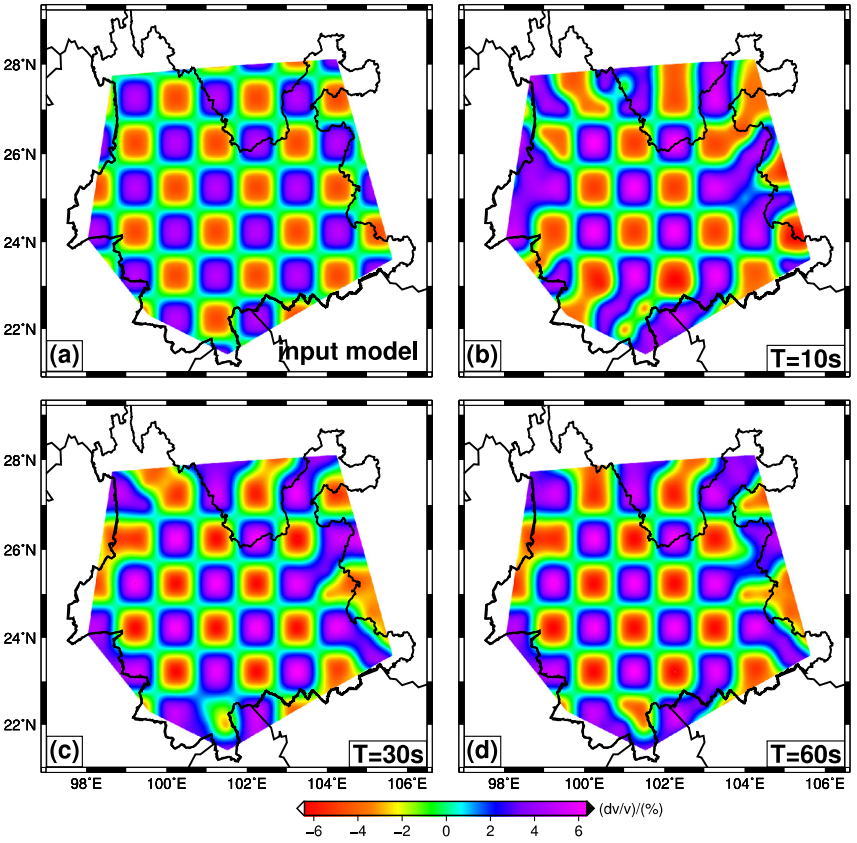

Fig. 8. Checkerboard tests for the raypath coverage at T = 10, 30 and 60 s. (a) Input model with ±6% velocity disturbance for 1° × 1° grids. (b–d) are inversion results of 10, 30 and 60 s, respectively.

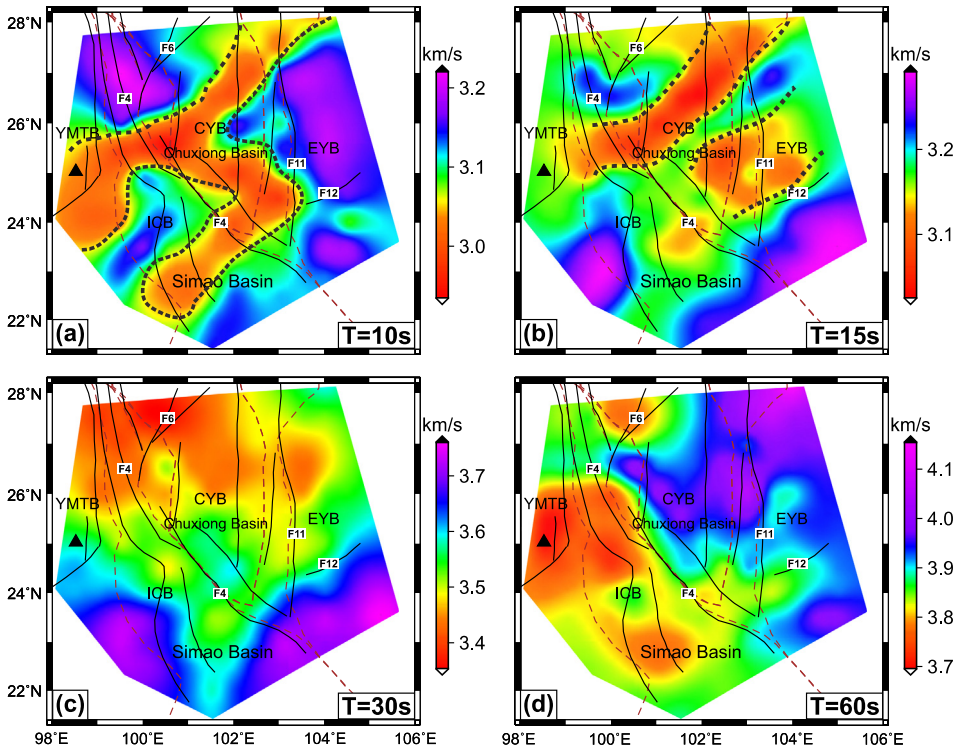

Fig. 9. Distribution images of the Rayleigh wave phase velocities at 10, 15, 30 and 60 s. The black triangle is the center of the TCVF. The brown dotted lines divide the study region into four blocks, which are the YMTB, ICB, CYB, and EYB. In addition, the F4: RRF, F6: LJNLF, F11: XJF and F12: MLSZF are used to interpret the distribution features of the phase velocity anomaly. At 10 s and 15 s, the area delineated by black dotted lines is a prominent low-velocity anomaly belt.

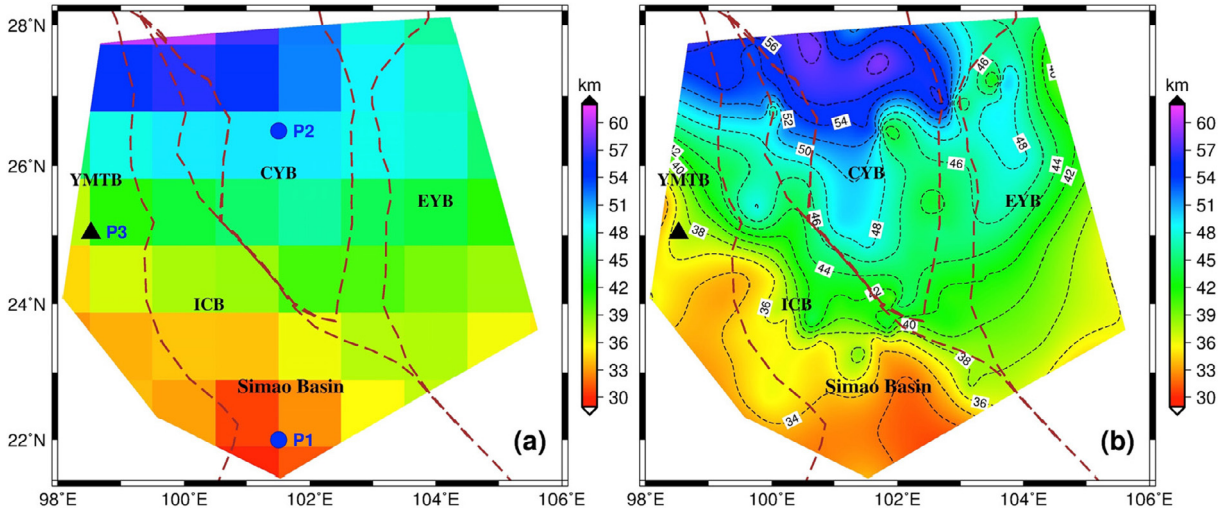

Fig. 10. Crustal thickness models of the SE margin of the Tibetan Plateau. (a) CRUST 1.0 model derived from Laske et al. (2013). The blue point P1, P2 and black triangle P3 are located in different block units. Point P1 (101.5°E, 22°N) is located in the south of SMB, while point P2 (101.5°E, 26.5°N) is located in the CYB and P3 (98.5°E, 25°N) is located at the center of the TCVF. The inverted results of the three test points are shown in Figs. 12 and 15b. (b) Receiver function model derived from Li et al. (2014b). (For interpretation of the references to colour in this figure legend, the reader is referred to the web version of this article.)

the checkerboard tests demonstrate that the two approaches are somewhat identical and it is reasonable to divide the study region into 0.5° × 0.5° grids. The path coverage (Fig. 6) and resolution (Figs. 7 and 8) around the TCVF are sufficient at 30 s and 60 s to invert the phase velocity and S-wave velocity structure. Fig. 9 shows the phase velocity distribution maps of four typical periods.

2.4. Inversion of S-wave velocity structure

Among the current inversion methods of S-wave velocity structures from surface wave dispersions, the iterative linear inversion method (Julià et al., 2000; Herrmann and Ammon, 2002) is the most widely used technique. To test the impact of the crustal thickness on the S-wave velocity structure and the trade-off in between, we construct two different initial models in the SE margin of the Tibetan Plateau, M1 and M2, with different Moho depths. The Moho depth of M1 is derived from the CRUST 1.0 model (Fig. 10a), and the Moho depth of M2 is derived from the receiver function (Fig. 10b) by Li et al. (2014b). The two 3-D initial models comprised the crustal velocity structure from the CRUST 1.0 model (Laske et al., 2013) and the upper mantle velocity structure from the globe 1-D reference model AK135 (Kennett et al., 1995).

Ignoring the sediment layers due to the lack of short-period dispersion data (T < 10 s), we divide the crust into three layers: the upper crust, middle crust and lower crust. At the depths of the Moho interface to 100 km, there are six layers with the same layer of thickness. The other layer of thickness is 10 km for the depth below 100 km, as performed by Chen et al. (2014a).

The Rayleigh wave phase velocity is primarily sensitive to the S-wave velocity structure with the maximum sensitivity depth at ~1/3 of a given wavelength (Fu et al., 2010). The depth sensitivity kernels of the Rayleigh wave velocities at different periods are shown in Fig. 11. The phase velocity at 60 s is quite sensitive to the S-wave structure at depths of ~90–120 km, so we can obtain the S-wave velocity structure above ~120 km. To stabilize the inversion, appropriate weights and damping values must be carefully selected for each layer. As is well known, a high weight value indicates a high contribution of the layered S-wave velocity to the dispersion data but also implies a significant misfit of the inverted layered velocity at the same time. We set the same weight of 1.0 for the layers above 120 km, while the layer between 120 km and 160 km have decreasing weights from 0.9 to 0.1, and the deep layer is fixed at zero weight. During the inversion, the thickness, density and Vp/Vs in each layer are fixed, and only the S-wave velocity is inverted due to the nonsensitivity of the Rayleigh wave dispersion to the P-wave velocity and density. We first invert the 1-D S-wave velocity structure of the study region with a grid spacing of 0.5° × 0.5° using the initial models M1 and M2, respectively. The inversion procedure continues until the standard error of the dispersion curve misfits less than the tolerable error, ~0.015 km/s, and the maximum iteration number is set to 30. We adopt a slightly higher damping value of 10 to avoid an overshoot in the beginning two iterations and then 0.1 in the following iterations. Subsequently, we gather all 1-D profiles to construct a 3-D S-wave velocity structure of the region.

Aside from M1 and M2, we construct another 1-D initial M3 model to calculate the inverted results. Differing from M1 and M2 in the fixed Moho depth, M3 (Fig. 12a and b) prefers a thin layered model without a priori Moho depth. The M3 model is similar to AK135 (Kennett et al., 1995), except for the same velocity (~4.5 km/s) in the crust and upper mantle to avoid the assumption of a Moho depth in the starting model. The layer thickness varies with depth: 2 km in the top 50 km, 5 km at 50–100 km, and 10 km below 100 km depth. This inversion strategy is the same as that of Bao et al. (2011) and Chen et al. (2014a).

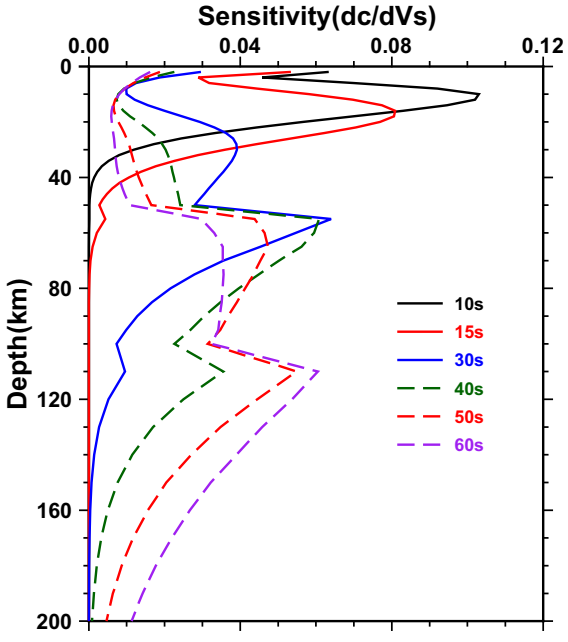

Fig. 11. Depth sensitivity kernels of the Rayleigh wave phase velocities at different periods. The kernels are calculated from the average velocity model of the SE margin of the Tibetan Plateau (Supplemental Fig. S1). Sensitivity of several periods (s) are plotted as functions of depth (km). At depths greater than ~120 km, surface waves begin to lose sensitivity due to their energy dissipation and attenuation.

3. Results

3.1. Phase velocity distribution

The phase velocity maps at periods of 10, 15, 30 and 60 s are shown in Fig. 9. The phase velocity distributions at certain periods directly reflect the lateral variation of the velocity structure at the corresponding depth range. The phase velocity distributions of 10 s and 15 s are quite sensitive to S-wave velocities in the upper-to-middle crust (~8–25 km depth; see Fig. 11), showing similar distribution features as the large-scale low-velocity anomalies. High-velocity anomalies exist around the Lijiang-Ninglang fault (LJNLF) and in the eastern Xiaojiang fault (XJF). Low-velocity zones appear in the Simao Basin (SMB), Chuxiong Basin (CXB), and the TCVF, while the spatial distribution of these low-velocity anomalies are shown as tube-shaped (marked by black dashed lines in Fig. 9a and b). In addition, at 15 s, low-velocity anomalies appear on both sides of the XJF, indicating that it is a fracture zone with a low maturity structure. According to the statistics, since 1500, over 10 earthquakes greater than Mw6.0 have taken place in and around the XJF.

The phase velocity distribution at 30 s reflects the S-wave velocity of the lower crust and crust-mantle transition zone (~50–60 km). The Sichuan-Yunnan diamond block, enclosed by the Red River fault (RRF), XJF, and LJNLF, show large-scale low-velocity anomalies (Wang et al., 2003; Wang and Gao, 2014). High-velocity anomalies appear in the southeastern and southwestern parts of the study region, which were also found in previous studies by ambient noise tomography (e.g., Wang and Gao, 2014). Such a large-scale low-velocity anomaly may imply that the presence of channel flow is at the crust-mantle boundary.

The phase velocity distribution at 60 s primarily reflects the S-wave velocity of the upper mantle (~90–120 km). Compared to short periods, the lateral variation of the phase velocity is smaller. The high-velocity anomalies are distributed in the Central Yunnan Block (CYB) and the northeastern part, while the low-velocity anomalies appear in the southwestern part and the vicinity of the Mile-Shizong fault (MLSZF).

3.2. 3-D S-wave velocity structures

To confirm the final inverted results, the influence of different initial models on the inversion results are tested at points P1, P2 and P3 Figs. 12 and 15b). Point P1 is located in the south of SMB, P2 is located in the CYB, and P3 is located at the center of the TCVF. Because the mean absolute difference value of the crustal thickness in M1 and M2 is ~1.6 km, we establish 20 different initial models with Moho depth varying in a range of [−1.6, 1.6] km from the initial M2 model is used at each point. M3 model is also used to contribute to the validation analysis. The inversion results of the three points are shown in Figs. 12 and 15b. It is noted that the inverted results are sensitive to the depth of the Moho interface. The inverted S-wave velocity structure of the initial M3 model is consistent with that of the initial models M1 and M2, which proves the validity of our inversion strategy. The inversion results of points P1, P2 and P3 show that the S-wave velocity structure varies with place. The overall crustal S-wave velocity at point P1 is higher than that of points P2 and P3. While the S-wave velocity structure

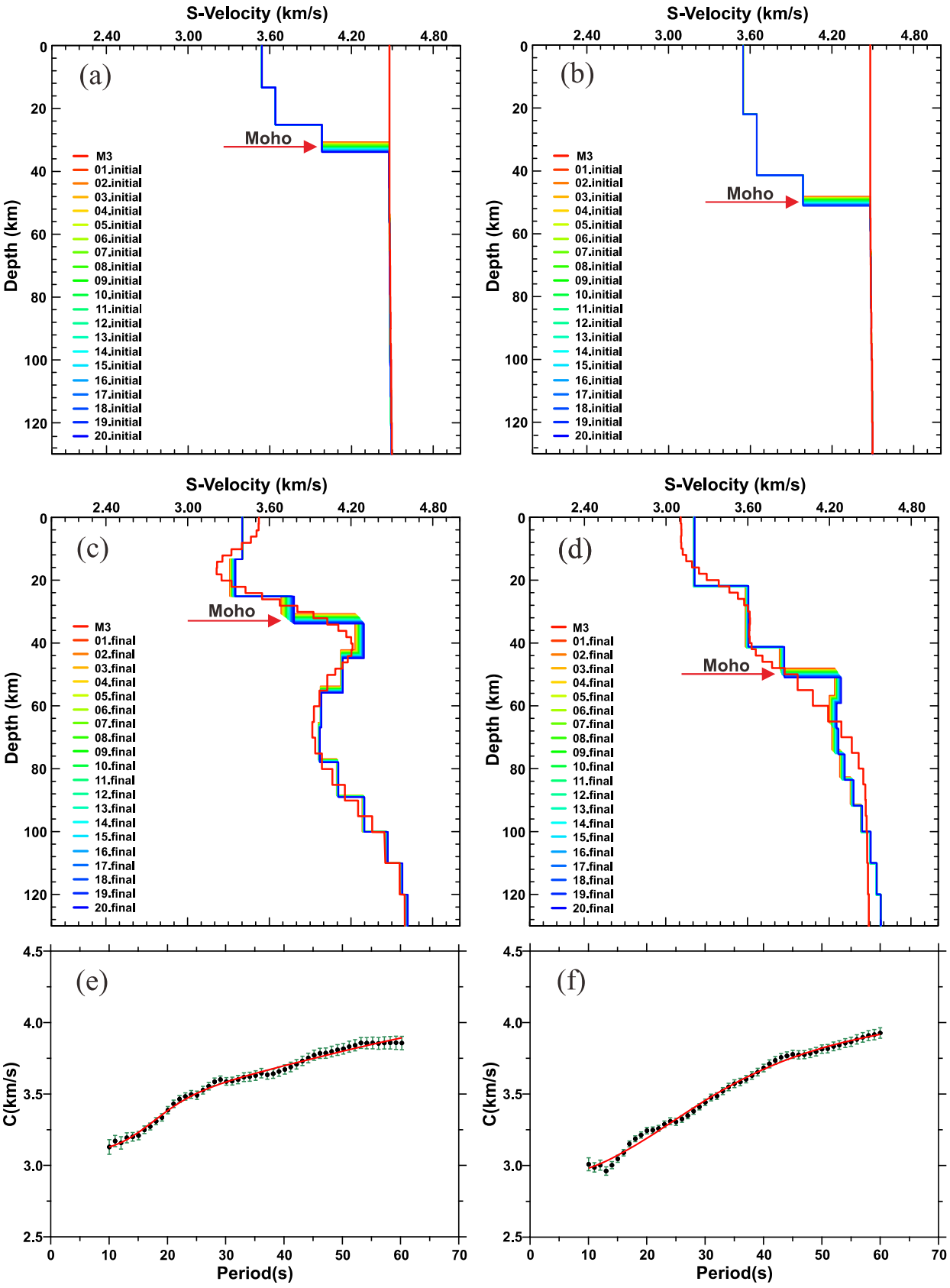

Fig. 12. Inverted results and data fit at points P1 and P2. The position of points P1 and P2 are shown in Fig. 10. (a) and (b) are the initial models of points P1 and P2, respectively. 1–20 are different initial models within the variation range of the Moho depth is [−1.6, 1.6] km, which are modified based on the initial M2 model. M3 is initial model without a priori Moho depth. (c) and (d) are the inverted S-wave velocity structure corresponding to (a) and (b). (e) and (f) denote the measured phase velocity curves (black dots) with error bars and the theoretical phase velocity curves (red solid line) calculated from the final models. (For interpretation of the references to colour in this figure legend, the reader is referred to the web version of this article.)

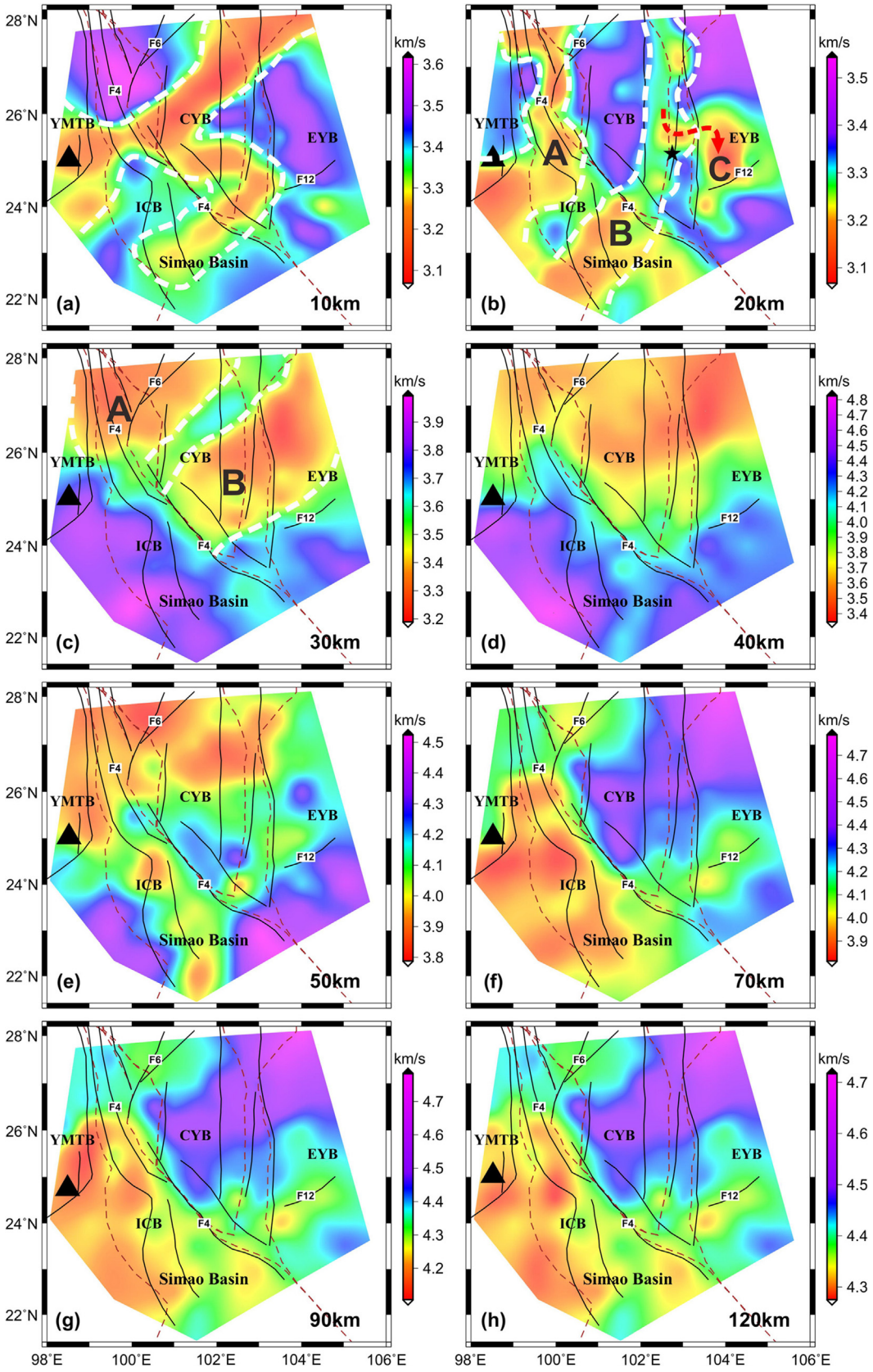

Fig. 13. The S-wave velocity structure of the SE margin of the Tibetan Plateau at different depths. The black triangle is the center of the TCVF. The area delineated by the white dotted lines in (a) is an "h-shaped" low-velocity anomaly belt. The black star denotes the location of the Kunming in (b). The white dashed lines in (b) and (c) are the boundaries of the two crustal flowing channels (marked with A and B). The red arrow indicates the branch of channel B (marked with C) in (b). For the full name of YMTB, ICB, CYB, and EYB, see in Fig. 1. In addition, the F4: RRF, F6: LJNLF and F12: MLSZF are used to explain the distribution features of the S-wave velocity. (For interpretation of the references to colour in this figure legend, the reader is referred to the web version of this article.)

at point P1 is similar to that of point P3, there are obvious low-velocity anomalies in the middle crust and upper mantle. Previous studies have indicated the presence of low-velocity anomalies in the crust that extends downward to the upper mantle of this region (Huang et al., 2002; Li et al., 2008b; Yao et al., 2010; Chen et al., 2014b; Bao et al., 2015).

The S-wave velocity structures of the SE margin of the Tibetan Plateau at depths of 30, 60 and 120 km that are inverted from three different starting models (i.e., M1, M2 and M3) are shown in Supplemental Fig. S2. We find the main features of the inversion results at depths consistent with three different initial models, which prove the stability and reliability of our inversion results. Finally, the 3-D S-wave velocity structure inverted from the initial M3 model is depicted in Fig. 13. The 3-D images clearly reveal the lateral variations of the S-wave velocity in the crust and upper mantle. It is characterized by a changeable Moho depth and the extensive distribution of low-velocity anomalies (Figs. 13 and 14). In addition, two representative vertical cross-sections of the S-wave velocity structure from the surface down to 120 km are shown in Fig. 14, displaying the complex distribution of low-velocity anomalies in the study region.

At a depth of 10 km, the S-wave velocity shows a strong correlation with the Rayleigh wave phase velocity at 10 s. The spatial distribution of low-velocity anomalies is characterized by an "h-shaped". The CYB and SMB show significant low-velocity anomalies, while high-velocity anomalies appear in the East Yunnan Block (EYB) and around the LJNLF. In addition, there is an obvious low-velocity anomaly in the vicinity of the TCVF, which is probably related to regional complex geological and magmatic activity. At a depth of 20 km, the prominent feature is the clear existence of the two low-velocity channels (see Fig. 13b, marked as A and B), and both rotate clockwise around the Eastern Himalaya Syntaxis (EHS). Our results are consistent with the fast-wave polarization direction from the local S-wave splitting (Shi et al., 2006), the azimuth anisotropy from the Rayleigh waves (Lu et al., 2014), and the velocity field from the GPS observation (Gan et al., 2007). Channel A extends toward the southwest, while channel B extends first toward the south and then toward the SMB. We also find that channel B has a branch north of Kunming, which flows to the vicinity of the MLSZF (Fig. 13b). At a depth of 30 km, the two channels still exist, and the channel diameter is increased. However, they are mainly distributed in the northern part of the RRF (Fig. 13c). Our results at 20 km and 30 km are similar to those of Bao et al. (2015) for 21 km and 31 km. At a depth of 40 km, the S-wave velocity shows great similarity with the phase velocity distribution at 30 s. There is a continuously distributed low-velocity zone in the northern part of the region, which reflects that the depth of the low-velocity layer is deeper than in the southern part; that is, the crust in the northern part is thicker than that of southern part of the study region (Li et al., 2014b). At a depth of 50 km, the velocity distribution becomes complicated in the crust-mantle transition zone (Fig. 13e). Low-velocity anomalies appear in the CYB, Indo-China Block (ICB), and TCVF. Compared with the results at depths of 30 km, 40 km and 50 km, the range of the high-velocity anomaly is gradually shrinking in the southwestern part. At depths of 70 km, 90 km and 120 km, the S-wave velocity distributions are quite similar. Their S-wave velocities show a strong correlation with the phase velocity distribution at 60 s. The southwest side of the RRF shows a low-velocity anomaly, while the CYB and the northeast side of the RRF shows a high-velocity anomaly. The low-velocity anomaly mainly exists in the TCVF and SMB, which may be related to the upwelling of the deep asthenosphere. In addition, the S-wave velocity distribution patterns in the northeastern and southwestern parts of the region are distinctly different, and the RRF acts as the boundary between two sides (Fig. 13f, g and h) and may reflect the difference of rock physical properties on both sides. The RRF may have cut through the whole crust and extended down to the upper mantle (Huang et al., 2002; Lei et al., 2009). The vicinity of the MLSZF manifests as a low-velocity feature, which may be connected to deep geothermal activity and performs the conduction and convection process that allows the formation of the regional geothermal anomaly.

Fig. 14 shows the vertical cross-sections of the S-wave velocity structure along the two profiles shown in Fig. 1a; profile a-b is

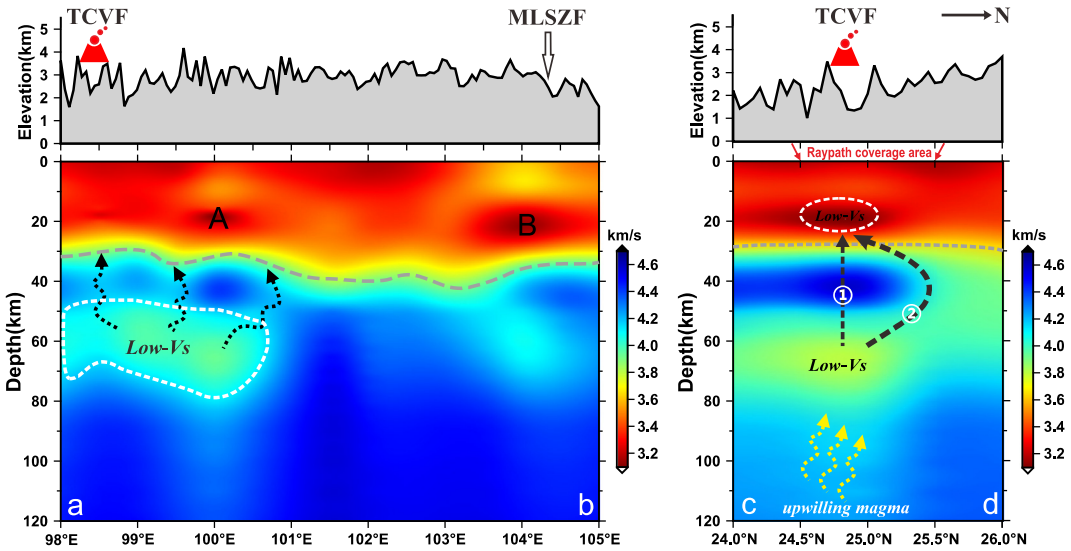

Fig. 14. Vertical cross-sections of the S-wave velocity structure along the two profiles shown in Fig. 1a. Profile a-b is along 25.0°N and profile c-d is along 98.5°E. The red triangle and red circle denote the location of the TCVF. Gray dotted lines represent the estimated Moho. A and B denote two channels of low-velocity anomalies as shown in profile a–b. The white dashed polygon denotes the boundary of low-velocity anomaly. The black dotted arrows represent the main migration pathways of magmatic material from the upper-mantle to the crust. The area between 24.5°N and 25.5°N is an effective range of raypath coverage in c–d profile. White dashed ellipses indicate the low-velocity anomaly in the crust of the TCVF. In this paper, low-velocity is interpreted as magma chambers (Tanaka et al., 2002; Lees, 2007). Two black dashed arrows (marked with ①, ②) denote two different migration patterns of magmatic material from the upper-mantle to the crust. The yellow dotted arrows indicate the upwelling pathways of magmatic material from the deep mantle-derived melts. In the top right corner, N represents the direction of the profile. The elevation surface topography along the profile is shown above the cross-section. (For interpretation of the references to colour in this figure legend, the reader is referred to the web version of this article.)

along 25.0°N and profile c-d is along 98.5°E. For profile a-b, there are obviously two low-velocity zones, A and B, in the crust. Anomaly B (~15–25 km) is deeper than anomaly A (~15–20 km), and they are independent of each other. The Moho depth changes slightly in the east-west direction. The upper mantle of the TCVF, which is at a depth of ~50–80 km, with a lateral extent of approximately 200 km, displays a prominent low-velocity anomaly. This provides powerful evidence for the lateral migration of magmatic material from the upper mantle to the crust. For profile c–d, we also observe two low-velocity anomalies beneath the TCVF, which are distributed in the crust (~15–25 km) and upper mantle (~50–80 km), and a high-velocity anomaly (~35–50 km) located between the two low-velocity anomalies. Petrologic and geochemical studies show that the magma of the TCVF originates in the upper mantle (Du et al., 2005). Thus, the formation of low-velocity anomalies in the crust is may be caused by two different migration patterns of magmatic materials. One migration pattern is upward migration by crack seepage (① in Fig. 14; profile c–d), and the other is lateral migration from upper mantle magmatic material (② in Fig. 14; profile c–d), where ② is the main migration pathway from the upper mantle to the crust. The formation of a high-velocity anomaly may be related to solidified magma intrusions and residual magma within the cooled volcanic material channel. It is fascinating to analyze the dynamic activities of the Tengchong volcano when examining these results concerning with chronological and spatial information.

4. Discussions

4.1. Two flowing channels in the SE margin of the Tibetan Plateau

Our inverted 3-D S-wave velocity model shows the existence of two low-velocity zones (Fig. 13b and c) in the crust of the SE margin of the Tibetan Plateau. This implies the presence of low-viscosity weak material in the crust (Royden, 1996; Bai et al., 2010). The two zones were also found in previous magnetotelluric imaging (Bai et al., 2010), Lg-wave attenuation tomography (Zhao et al., 2013), ambient-noise adjoint tomography (Chen et al., 2014b), and the joint inversion of surface wave dispersion and receiver functions (Sun et al., 2014; Bao et al., 2015; Li et al., 2016). However, the depth distribution and connectivity of the two channels are still being controversial.

Using the magnetotelluric image approach, Bai et al. (2010) found two zones or channels with high conductivity at depths of ~20–40 km, which were interpreted as channels of crustal flow. Zhao et al. (2013) found two different depth channels of crustal flow by Lg-wave attenuation tomography. They believed that the main flow channel first comes from north and moves eastward and then turns toward SE Tibet. Another channel starts from southern Tibet, crosses the EHS, and eventually merges with the main flow channel. Chen et al. (2014b) found two disconnected low-velocity channels in the crust of SE Tibet through ambient-noise adjoint tomography. Bao et al. (2015) observed two crustal low-velocity channels in SE Tibet, and the two channels are at 10–20 km and 20–30 km in depth, respectively. Li et al. (2016) also found two channels distributed at depths of ~20–25 km and ~20–30 km, and they are connected in the southern region of the SE Tibetan Plateau. Our inversion results show that the two channels, A and B, are located at ~15–20 km and ~15–25 km depth, respectively (Figs. 13b, c and 14). Channel A extends toward the southwest, while channel B extends south first and then toward the SMB (Fig. 13b). These results are similar in both location and depth to the finding obtained by Bao et al. (2015) and Li et al. (2016). However, there are still some differences. First, we find that channel B has a short branch north of Kunming, part of which flows to the southwestern part (marked by B in Fig. 13b), and the other part flows into the vicinity of the MLSZF (marked by C in Fig. 13b). In addition, our results demonstrate that the two low-velocity channels are connected in the middle-to-lower crust (~20 km; Fig. 13b) and separate in the lower crust (~30 km; Fig. 13c), which also has been found in previous studies (Zhao et al., 2013; Li et al., 2016).

4.2. Dynamic model of the Tengchong volcanic magmatic system

The TCVF is located in the western region of the SE Tibetan Plateau and is close to the China-Burma border. Approximately 70 volcanoes are distributed along a N-S trend (Xu et al., 2012). Geothermal activity and crustal earthquakes often occur in this area (Wang and Huangfu, 2004). In this study, we add the tomographic data recorded by the Tengchong volcano Monitoring Network, providing higher resolution to invert the reliable S-wave velocity structure underneath the TCVF. In past decades, various geophysical methods were used to investigate the crust-mantle structure and dynamic mechanisms of the TCVF (Liu et al., 1993; Qin et al., 2000; Huang et al., 2002, 2015; Huang and Zhao, 2006; Zhao et al., 2006; Gao et al., 2008; Lei et al., 2009; Zhao and Liu, 2010; Yang et al., 2011; Xu et al., 2012; Zhou et al., 2012; Zhang et al., 2016). Qin et al. (2000) found two low-velocity anomalies at depths of ~3–9 km and ~15–24 km beneath the TCVF using the local P-wave tomography. These two low-velocity anomalies most likely represent magma chambers or areas of partial melting. The results of Yang et al. (2011) and Xu et al. (2012) revealed an obvious low-velocity anomaly at a depth of 10–20 km with a lateral extent of ~20–30 km. They speculated that this low-velocity anomaly represents the magma and heat source of the volcanic eruptions during the Pleistocene and Holocene eras. In teleseismic P-wave receiver function studies, Gao et al. (2008) found a prominent low-velocity anomaly that was approximately ~10–20 km thick beneath the TCVF. Liu et al. (1993) found that a low-velocity plume existed at a depth of 25–110 km, which was caused by mantle upwelling. Tomographic studies on SE Tibet and southwestern China also identified the presence of low-velocity anomalies in the crust and upper mantle of the TCVF, which may relate to magmatic activities (Wang et al., 2003, 2014). In addition, according to the relative geothermal gradient, Zhao et al. (2006) speculated that three magma chambers exist beneath the TCVF, with a lateral extent of ~19–28 km and a depth of ~4–12 km or more.

Combining previous studies with our inverted S-wave velocity structure in the TCVF, we propose a magma transport model (Fig. 15a). The basic explanation for this model is that the magma of the Tengchong volcanoes mainly comes from the deep mantle-derived melts. The underthrusting of the ridge along the 410 km discontinuity (Zhou et al., 2012) or the Indian plate along the 660 km discontinuity (Zhao and Liu, 2010) beneath the Eurasian plate may cause the volcanic eruptions. The magma originates from the deeper mantle, and then migrates through upward crack seepage and lateral magma conduit flows or along the lithospheric fault systems. Fig. 14 profile c–d and Fig. 15b clearly show the S-wave velocity structure in the TCVF. There are two obvious low-velocity anomalies (~15–25 km and ~50–80 km) and a high-velocity anomaly (~35–50 km). A noticeable low-velocity anomaly exists in the crust, which was also found in previous P-wave tomographic studies (Qin et al., 2000; Gao et al., 2008; Yang et al., 2011; Xu et al., 2012). They inferred that the low-velocity anomaly in the crust was perhaps a residual magma chamber or partially molten material. This low-velocity anomaly may represent magmatic activity and could even affect the regional geothermal anomaly. In addition, at 20 km depth (Fig. 13b), the low-velocity channel A extends to the TCVF, and a prominent low-velocity anomaly appears in the middle-to-lower crust (~20 km) of the TCVF

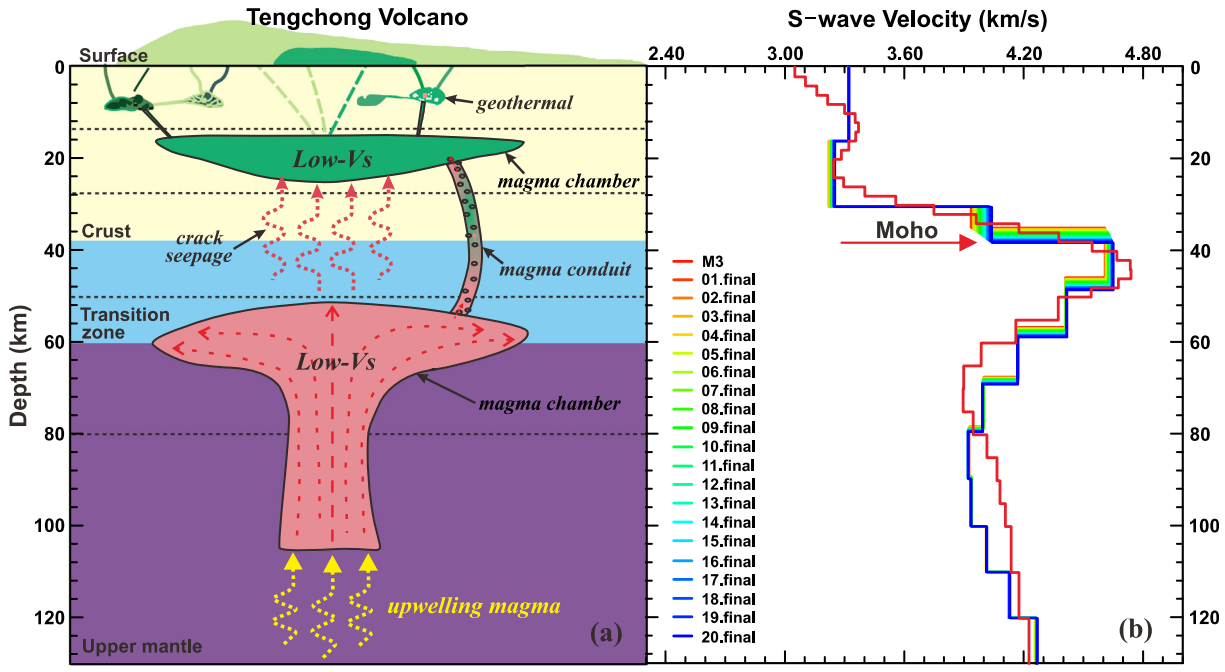

Fig. 15. (a) A schematic cartoon showing the magma dynamics model of the TCVF. (b) The S-wave velocity structure profile from the inversion of phase dispersion curve at the node corresponding to the black triangle (see Fig. 10 point P3). 21 different inversion results are derived from the different initial models are shown in Supplemental Fig. S3. The variation range of the Moho depth is [−1.6,1.6] km, which are modified based on the initial M2 model. The red solid line is the inversion result of the initial M3 model that without priori Moho depth. (For interpretation of the references to colour in this figure legend, the reader is referred to the web version of this article.)

(Fig. 14 profile c–d, and Fig. 15). Channel A is connected with the magmatic material in the crust of the TCVF, and they may interact with each other. Below the low-velocity anomaly (~15–25 km), a high-velocity anomaly exists at a depth of ~30–50 km, which may relate to the high-density material formed by cooled magma and solidified magma intrusions in the early period (Tanaka et al., 2002). Furthermore, a low-velocity anomaly is also found in the upper mantle at depths of ~50–80 km. It is still unclear how this low-velocity anomaly was generated. There may be three possible causes for this low-velocity anomaly. The first possibility is caused by the upwelling of hot mantle material from the deeper mantle. Petrologic and geochemical study results support the existence of this possibility (Du et al., 2005). Low-velocity anomalies under volcanoes are interpreted as evidence for magma accumulation, whereas many high-velocity anomalies are commonly interpreted as older remnant magma systems that have cooled and solidified (Tanaka et al., 2002; Lees, 2007). The second possibility is caused by the existence of residual magma, which has not cooled or solidified in the lithospheric fault systems. Zhou et al. (2012) believed that the Tengchong volcanism may be related to the flatter Ninety East Ridge subduction. Wei et al. (2012) found that the Tengchong volcanism may related to the subduction of the Burma microplate under the Eurasian plate. Thus, we speculate that the third possibility is associated with the upward moving of the deep mantle-derived melts, which is caused by the ridge subduction along the ~410 km discontinuity or the eastward subduction of the Indian plate under the Eurasian plate. Thus far, our inverted S-wave velocity model obtained by surface wave tomography provides more details about the Tengchong volcanic activities relative to current models.

5. Conclusions

In this study, we built a 3-D S-wave velocity structure model of the crust and upper mantle (10–120 km) beneath the SE margin of the Tibetan Plateau by inverting the phase velocities of the Rayleigh wave from the surface wave tomography. The resulting 3-D tomographic model provides new insights into the two crustal flowing areas of the region and their relation to the Tengchong volcanic magma chambers.

The model reveals two low-velocity channels for crustal flowing beneath the SE margin of the Tibetan Plateau and two prominent low-velocity anomalies under the TCVF. The features of two low-velocity channels are summarized as follows: (1) They exhibit a clockwise rotation around the EHS. Channel A is connected with the magmatic material in the crust of the TCVF, and channel B has a branch. (2) The two low-velocity channels connect in the middle-to-lower crust and separate in the lower crust. Our results suggest that the region is a non-uniform passageway of the Plateau material moving southeast, which indicates that the Plateau deformation occurs not only at the surface but also in the deep crust.

Additionally, we propose a dynamic model of the TCVF magma system inferred from the 3-D S-wave velocity structure. We find that the magmatic activity in the TCVF may interact with one of the crustal flowing channels in the SE margin of the Tibetan Plateau. Although the dynamic mechanism of magmatic activity has become clearer through our results, more geoscience studies for the origin of magma chambers and material migration within the crust-mantle are still needed.

Acknowledgements

We would like to thank the Earthquake Administration of Yunnan Province for providing the seismic waveform data. We greatly thank the Editor-in-Chief, Professor Meifu Zhou, and anonymous reviewers for their constructive comments and suggestions that improve this manuscript. We thank Prof. Huajian Yao and T.B. Yanovskaya for providing computer software. This study were supported by the National 973 Project of China (No. 2013CB733303), the National Natural Science Foundation of China (No. 41474093), the Key Natural Science Foundation of Hubei Province (No. 2014CFA110) and the open fund of Key Laboratory of

Geospace Environment and Geodesy, Ministry of Education (No. 15-02-07). Most of the figures were prepared using Generic Mapping Tools (GMT).

Appendix A. Supplementary material

Supplementary data associated with this article can be found, in the online version, at http://dx.doi.org/10.1016/j.jseaes.2016.09.017.

References

Bai, D.H., Unsworth, M.J., Meju, M.A., Ma, X.B., Teng, J.W., Kong, X.R., Sun, Y., Sun, J., Wang, L.F., Jiang, C.S., Zhao, C.P., Xiao, P.F., Liu, M., 2010. Crustal deformation of the eastern Tibetan plateau revealed by magnetotelluric imaging. Nat. Geosci. 3 (5), 358–362.

Bao, X.W., Xu, M.J., Wang, L.S., Mi, N., Yu, D.Y., Li, H., 2011. Lithospheric structure of the Ordos Block and its boundary areas inferred from Rayleigh wave dispersion. Tectonophysics 499 (1), 132–141.

Bao, X.W., Sun, X.X., Xu, M.J., Eaton, D.W., Song, X.D., Wang, L.S., Ding, Z.F., Mi, N., Li, H., Yu, D.Y., Huang, Z.C., Wang, P., 2015. Two crustal low-velocity channels beneath SE Tibet revealed by joint inversion of Rayleigh wave dispersion and receiver functions. Earth Planet. Sci. Lett. 415, 16–24.

Chen, H.P., Zhu, L.B., Wang, Q.D., Zhang, P., Yang, Y.H., 2014a. S-wave velocity structure of the North China from inversion of Rayleigh wave phase velocity. J. Asian Earth Sci. 88, 178–191.

Chen, M., Huang, H., Yao, H.J., Hilst, R.D.V.D., Niu, F.L., 2014b. Low wave speed zones in the crust beneath SE Tibet revealed by ambient noise adjoint tomography. Geophys. Res. Lett. 41 (2), 334–340.

Clark, M.K., Royden, L.H., 2000. Topographic ooze: building the eastern margin of Tibet by lower crustal flow. Geology 28 (8), 703–706.

Cook, K.L., Royden, L.H., 2008. The role of crustal strength variations in shaping orogenic plateaus, with application to Tibet. J. Geophys. Res.: Solid Earth 113 (B8).

Danesi, S., Morelli, A., 2001. Structure of the upper mantle under the Antarctic Plate from surface wave tomography. Geophys. Res. Lett. 28 (23), 4395–4398.

DeCelles, P.G., Robinson, D.M., Zandt, G., 2002. Implications of shortening in the Himalayan-fold-thrust belt for uplift of the Tibetan Plateau. Tectonics 21 (6).

Deschamps, F., Lebedev, S., Meier, T., Trampert, J., 2008. Azimuthal anisotropy of Rayleigh-wave phase velocities in the east-central United States. Geophys. J. Int. 173 (3), 827–843.

Ditmar, P.G., Yanovskaya, T.B., 1987. A Generalization of Backus-Gilbert method for estimation of lateral variations of surface wave velocities. Izv. Phys. Solid Earth 23 (6), 470–477.

Du, J.G., Liu, C.Q., Fu, B.H., Ninomiya, Y., Zhang, Y.L., Wang, C.Y., Wang, H.L., Sun, Z.G., 2005. Variations of geothermometry and chemical-isotopic compositions of hot spring fluids in the Rehai geothermal field, southwestern China. J. Volcanol. Geoth. Res. 142 (3), 243–261.

England, P., Houseman, G., 1986. Finite strain calculations of continental deformation: 2. Comparison with the India-Asia collision zone. J. Geophys. Res.: Solid Earth 91 (B3), 3664–3676.

Fan, W.Y., Chen, Y.S., Tang, Y.C., Zhou, S.Y., Feng, Y.G., Yue, H., Wang, H.Y., Jin, G., Wei, S.Q., Wang, Y.B., Gai, Z.X., Ning, J.Y., 2015. Crust and upper mantle velocity structure of the eastern Tibetan Plateau and adjacent regions from ambient noise tomography. Chinese J. Geophys. 58 (5), 1568–1583.

Fang, L.H., Wu, J.P., Ding, Z.F., Panza, G.F., 2010. High resolution Rayleigh wave group velocity tomography in North China from ambient seismic noise. Geophys. J. Int. 181 (2), 1171–1182.

Fu, Y.V., Li, A.B., Chen, Y.J., 2010. Crustal and upper mantle structure of southeast Tibet from Rayleigh wave tomography. J. Geophys. Res.: Solid Earth 115, B12323.

Gao, X., Guo, Z., Wang, W.M., Yao, Z.X., 2008. Crustal structure beneath Tengchong-Lincang region, Yunnan province, revealed by transform function. Chinese J. Geophys. 51 (2), 451–459.

Gan, W.J., Zhang, P.Z., Shen, Z.K., Niu, Z.J., Wang, M., Wan, Y.G., Zhou, D.M., Cheng, J., 2007. Present-day crustal motion within the Tibetan Plateau inferred from GPS measurements. J. Geophys. Res.: Solid Earth 112 (B08416), 582–596.

He, Z.Q., Ye, T.L., Su, W., 2004. S-wave velocity structure of the middle and upper crustal in the Yunnan region. Chinese J. Geophys. 47 (2), 838–844.

He, Z.Q., Ye, T.L., Su, W., 2005. 3-D velocity structure of the middle and upper crust in the Yunnan region, China. Pure Appl. Geophys. 162 (12), 2355–2368.

Hansen, C., 1998. Rank-Deficient and Discrete Ill-Posed Problems. Numerical Aspects of Linear Inversion: Department of Mathematical Modeling. Technical University of Denmark, Lyngby, p. 247.

Herrmann, R.B., Ammon, C.J., 2002. Computer Programs in Seismology: Surface Wave, Receiver Function and Crustal Structure. Saint Louis University, St. Louis, MO, USA.

Huang, J.L., Zhao, D.P., Zheng, S.H., 2002. Lithospheric structure and its relationship to seismic and volcanic activity in southwest China. J. Geophys. Res.: Solid Earth 107 (B10). ESE 13-1–ESE 13-14.

Huang, J.L., Zhao, D.P., 2006. High-resolution mantle tomography of China and surrounding regions. J. Geophys. Res.: Solid Earth 111, B9305.

Huang, Z.X., Li, H.Y., Xu, Y., 2013. Lithospheric S-wave velocity structure of the North-South Seismic Belt of China from surface wave tomography. Chinese J. Geophys. 56 (4), 1121–1131.

Huang, Z.C., Wang, P., Xu, M.J., Wang, L.S., Ding, Z.F., Wu, Y., Xu, M.J., Mi, N., Yu, D.Y., Li, H., 2015. Mantle structure and dynamics beneath SE Tibet revealed by new seismic images. Earth Planet. Sci. Lett. 411, 100–111.

Julià, J., Ammon, C.J., Herrmann, R.B., Correig, A.M., 2000. Joint inversion of receiver functions and surface wave dispersion observations. Geophys. J. Int. 143, 99–112.

Kennett, B.L.N., Engdahl, E.R., Buland, R., 1995. Constraints on seismic velocities in the Earth from traveltimes. Geophys. J. Int. 122 (1), 108–124.

Laske, G., Masters, G., Ma, Z., Pasyanos, M., 2013. Update on CRUST1.0-A 1-degree global model of Earth's crust. Geophys. Res. Abstracts 15, 2658.

Lebedev, S., Nolet, G., 2003. Upper mantle beneath Southeast Asia from S velocity tomography. J. Geophys. Res.: Solid Earth 108 (B1), 2048.

Lees, J.M., 2007. Seismic tomography of magmatic systems. J. Volcanol. Geoth. Res. 167, 37–56.

Lei, J.S., Zhao, D.P., Su, Y.J., 2009. Insight into the origin of the Tengchong intraplate volcano and seismotectonics in southwest China from local and teleseismic data. J. Geophys. Res.: Solid Earth 114, B5302.

Levshin, A.L., Barmin, M.P., Ritzwoller, M.H., Trampert, J., 2005. Minor-arc and major-arc global surface wave diffraction tomography. Phys. Earth Planet. Inter. 149 (3), 205–223.

Li, C., Hilst, R.D.V.D., Meltzer, A.S., Engdahl, E.R., 2008a. Subduction of the Indian lithosphere beneath the Tibetan Plateau and Burma. Earth Planet. Sci. Lett. 274, 157–168.

Li, M.K., Zhang, S.X., Wang, F., Wu, T.F., Qin, W.B., 2016. Crustal and upper-mantle structure of the Southeastern Tibetan Plateau from joint analysis of surface wave dispersion and receiver function and its tectonic implications. J. Asian Earth Sci. 117, 52–63.

Li, S., Feng, M., An, M.J., Dong, S.W., 2014a. Azimuthal anisotropy of Rayleigh wave in Qinling and its adjacent areas. Acta Seimologica Sinica 36 (4), 531–545 (in Chinese with English Abstract).

Li, Y., Yao, H.J., Liu, Q.Y., Chen, J.H., Li, S.C., Huang, H., 2010. Phase velocity array tomography of Rayleigh waves in western Sichuan from ambient seismic noise. Chinese J. Geophys. 53 (4), 842–852.

Li, Y.H., Wu, Q.J., Zhang, R.Q., Tian, X.B., Zeng, R.S., 2008b. The crust and upper mantle structure beneath Yunnan from joint inversion of receiver functions and Rayleigh wave dispersion data. Phys. Earth Planet. Inter. 170 (1), 134–146.

Li, Y.H., Wu, Q.J., Pan, J.T., Zhang, F.X., Yu, D.X., 2013. An upper-mantle S-wave velocity model for East Asia from Rayleigh wave tomography. Earth Planet. Sci. Lett. 377, 367–377.

Li, Y.H., Gao, M.T., Wu, Q.J., 2014b. Crustal thickness map of the Chinese mainland from teleseismic receiver functions. Tectonophysics 611, 51–60.

Liu, R.F., Chen, P.S., Li, Q., 1993. Three-dimension velocity pictures in Yunnan and the surrounding regions. Acta Seismol. Sin. 15 (1), 61–67 (in Chinese).

Lu, L.Y., He, Z.Q., Ding, Z.F., Wang, C.Y., 2014. Azimuth anisotropy and velocity heterogeneity of Yunnan area based on seismic ambient noise. Chinese J. Geophys. 57 (3), 822–836.

Molnar, P., Tapponnier, P., 1975. Cenozoic tectonics of Asia: effects of a continental collision. Science 189 (4201), 419–426.

Ni, J.F., Guzman-Speziale, M., Bevis, M., Holt, W.E., Wallace, T.C., Seager, W.R., 1989. Accretionary tectonics of Burma and the three-dimensional geometry of the Burma subduction zone. Geology 17 (1), 68–71.

Pan, J.T., Li, Y.H., Wu, Q.J., Ding, Z.F., 2015. Phase velocity maps of Rayleigh waves in the southeast Tibetan plateau. Chinese J. Geophys. 58 (11), 3993–4006 (in Chinese with English Abstract).

Qiao, X., Wang, Q., Rui-Lin, D.U., 2004. Current crustal deformation characteristics of active blocks in the Sichuan-Yunnan Region, China. Chinese J. Geophys. 47 (5), 908–915.

Qin, J.Z., Huang, P.G., Li, Q., Qian, X.D., Su, Y.J., Cai, M.J., 2000. 3-D chromatography of velocity structure in Tengchong volcano areas and nearby. Seismol. Res. 23 (2), 157–163 (in Chinese with English Abstract).

Ritzwoller, M.H., Levshin, A.L., 1998. Eurasian surface wave tomography: group velocities. J. Geophys. Res.: Solid Earth 103 (B3), 4839–4878.

Rowley, D.B., 1996. Age of initiation of collision between India and Asia: a review of stratigraphic data. Earth Planet. Sci. Lett. 145 (1), 1–13.

Royden, L., 1996. Coupling and decoupling of crust and mantle in convergent orogens: implications for strain partitioning in the crust. J. Geophys. Res.: Solid Earth 101 (B8), 17679–17705.

Royden, L.H., Burchfiel, B.C., van der Hilst, R.D., 2008. The geological evolution of the Tibetan Plateau. Science 321 (5892), 1054–1058.

Schoenbohm, L.M., Whipple, K.X., Burchfiel, B.C., Chen, L., 2004. Geomorphic constraints on surface uplift, exhumation, and plateau growth in the Red River region, Yunnan Province, China. Geol. Soc. Am. Bull. 116 (7–8), 895–909.

Shapiro, N.M., Campillo, M., Stehly, L., Ritzwoller, M.H., 2005. High-resolution surface-wave tomography from ambient seismic noise. Science 307 (5715), 1615–1618.

Shen, J., Wang, Y.P., Song, F.M., 2003. Characteristics of the active Xiaojiang fault zone in Yunnan, China: a slip boundary for the southeastward escaping Sichuan-Yunnan Block of the Tibetan Plateau. J. Asian Earth Sci. 21 (10), 1085–1096.

Shi, Y.T., Gao, Y., Wu, J., Luo, Y., Su, Y.J., 2006. Seismic anisotropy of the crust in Yunnan, China: polarizations of fast shear-waves. Acta Seismol. Sin. 28 (6), 574–585.

Simons, F.J., Zielhuis, A., van der Hilst, R.D., 1999. The deep structure of the Australian continent from surface wave tomography. Lithos 48 (1), 17–43.
Sun, X.X., Bao, X.W., Xu, M.J., Eaton, D.W., Song, X.D., Wang, L.S., Ding, Z.F., Mi, N., Yu, D.Y., Li, H., 2014. Crustal structure beneath SE Tibet from joint analysis of receiver functions and Rayleigh wave dispersion. Geophys. Res. Lett. 41 (5), 1479–1484.
Tanaka, S., Hamaguchi, H., Nishimura, T., Yamawaki, T., Ueki, S., Nakamichi, H., Tsutsui, T., Miyamachi, H., Matsuwo, N., Oikawa, J., Ohminato, T., Miyaoka, K., Onizawa, S., Mori, T., Aizawa, K., 2002. Three-dimensional P-wave velocity structure of Iwate volcano, Japan from active seismic survey. Geophys. Res. Lett. 29 (10), 59.
Tapponnier, P., Peltzer, G., Le Dain, A.Y., Armijo, R., Cobbold, P., 1982. Propagating extrusion tectonics in Asia: new insights from simple experiments with plasticine. Geology 10 (12), 611–616.
Tapponnier, P., Xu, Z.Q., Roger, F., Meyer, B., Arnaud, N., Wittlinger, G., Yang, J.S., 2001. Oblique stepwise rise and growth of the Tibet Plateau. Science 294 (5547), 1671–1677.
Wang, C.Y., Chan, W.W., Mooney, W.D., 2003. Three-dimensional velocity structure of crust and upper mantle in southwestern China and its tectonic implications. J. Geophys. Res.: Solid Earth 108, 176–193.
Wang, C.Y., Huangfu, G., 2004. Crustal structure in Tengchong volcano-geothermal area, western Yunnan. China. Tectonophys. 380 (1), 69–87.
Wang, Q., Gao, Y., 2014. Rayleigh wave phase velocity tomography and strong earthquake activity on the southeastern front of the Tibetan Plateau. Sci. China: Earth Sci. 57 (10), 2532–2542.
Wang, W.L., Wu, J.P., Fang, L.H., 2012. High resolution Rayleigh wave phase velocity tomography in northern North China. Geophys. J. Int. 189 (1), 647–658.
Wang, W.L., Wu, J.P., Fang, L.H., Lai, G.J., Yang, T., Cai, Y., 2014. S wave velocity structure in southwest China from surface wave tomography and receiver functions. J. Geophys. Res.: Solid Earth 119 (2), 1061–1078.
Wei, W., Xu, J.D., Zhao, D.P., Shi, Y.L., 2012. East Asia mantle tomography: new insight into plate subduction and intraplate volcanism. J. Asian Earth Sci. 60, 88–103.
Wei, W.B., Unsworth, M., Jones, A., Booker, J., Tan, H.D., Nelson, D., Chen, L.S., Li, S.H., Solon, K., Bedrosian, P., Jin, S., Deng, M., Ledo, J., Kay, D., Roberts, B., 2001. Detection of widespread fluids in the Tibetan crust by magnetotelluric studies. Science 292 (5517), 716–719.
Xu, Y., Yang, X.T., Li, Z.W., Liu, J.H., 2012. Seismic structure of the Tengchong volcanic area southwest China from local earthquake tomography. J. Volcanol. Geoth. Res. 239, 83–91.
Yao, H.J., Xu, G.M., Zhu, L.B., Xiao, X., 2005. Mantle structure from inter-station Rayleigh wave dispersion and its tectonic implication in western China and neighboring regions. Phys. Earth Planet. Inter. 148 (1), 39–54.
Yao, H.J., van der Hilst, R.D., Hoop, M.V.D., 2006. Surface-wave array tomography in SE Tibet from ambient seismic noise and two-station analysis—I. Phase velocity maps. Geophys. J. Int. 166 (2), 732–744.
Yao, H.J., Beghein, C., van der Hilst, R.D., 2008. Surface wave array tomography in SE Tibet from ambient seismic noise and two-station analysis—II. Crustal and upper-mantle structure. Geophys. J. Int. 173 (1), 205–219.
Yao, H.J., van der Hilst, R.D., Montagner, J.P., 2010. Heterogeneity and anisotropy of the lithosphere of SE Tibet from surface wave array tomography. J. Geophys. Res.: Solid Earth 115, B12307.
Yang, X.T., Xu, Y., Liu, J.H., Li, Z.W., 2011. Seismic tomography in the Tengchong volcanic area and its tectonic implication. Chinese J. Geophys. 54 (8), 2050–2059.
Yanovskaya, T.B., Ditmar, P.G., 1990. Smoothness criteria in surface wave tomography. Geophys. J. Int. 102 (1), 63–72.
Yanovskaya, T.B., 1997. Resolution estimation in the problems of seismic ray tomography, Izvestiya. Phys. Solid Earth 33 (9), 762–765.
Yanovskaya, T.B., Kizima, E.S., Antonova, L.M., 1998. Structure of the crust in the Black Sea and adjoining regions from surface wave data. J. Seismolog. 2 (4), 303–316.
Yin, A., Harrison, T.M., 2000. Geologic evolution of the Himalayan-Tibetan orogen. Annu. Rev. Earth Planet. Sci. 28 (1), 211–280.
Yu, D.X., Wu, Q.J., Wang, P., Ye, Q.D., Pan, J.T., He, J., Gao, M.T., 2016. Love wave phase velocity tomography in the south-central Mongolia from earthquakes. Acta Seismol. Sin. 38 (1), 41–52 (in Chinese with English Abstract).
Zhang, M.L., Guo, Z.F., Sano, Y.J., Zhang, L.H., Sun, Y.T., Cheng, Z.H., Yang, T.F., 2016. Magma-derived CO_2 emissions in the Tengchong volcanic field, SE Tibet: Implications for deep carbon cycle at intra-continent subduction zone. J. Asian Earth Sci. 127, 76–90.
Zhang, X., Wang, Y.H., 2009. Crustal and upper mantle velocity structure in Yunnan, Southwest China. Tectonophysics 471 (3), 171–185.
Zhao, C.P., Ran, H., Chen, K.H., 2006. Present-day magma chambers in Tengchong volcano area inferred from relative geothermal gradient. Acta Petrol. Sinica 22 (6), 1517–1528 (in Chinese with English Abstract).
Zhao, D.P., 2009. Multiscale seismic tomography and mantle dynamics. Gondwana Res. 15 (3), 297–323.
Zhao, D.P., Liu, L., 2010. Deep structure and origin of active volcanoes in China. Geosci. Front. 1 (1), 31–44.
Zhao, D.P., Wei, W., Nishizono, Y., Inakura, H., 2011. Low-frequency earthquakes and tomography in western Japan: insight into fluid and magmatic activity. J. Asian Earth Sci. 42 (6), 1381–1393.
Zhao, L.F., Xie, X.B., He, J.K., Tian, X., Yao, Z.X., 2013. Crustal flow pattern beneath the Tibetan Plateau constrained by regional Lg-wave Q tomography. Earth Planet. Sci. Lett. 383 (4), 113–122.
Zhou, M.F., Robinson, P.T., Wang, C.Y., Zhao, J.H., Yan, D.P., Gao, J.F., Malpas, J., 2012. Heterogeneous mantle source and magma differentiation of quaternary arc-like volcanic rocks from Tengchong, SE margin of the Tibetan Plateau. Contrib. Miner. Petrol. 163 (5), 841–860.